Developments in the Built Environment 21 (2025) 100595

Contents lists available at ScienceDirect

Developments in the Built Environment

journal homepage: www.sciencedirect.com/journal/developments-in-the-built-environment

Enhancing sustainable utilization of iron-based alkaline solid wastes for carbon mineralization: Insights into CO_2 transport and adsorption dynamics

Gen Li [a], Jie Yang [b], Hao Li [c], Jiaxiang Liew [a,*], Jiasheng Huang [a,**]

[a] Department of Civil and Environmental Engineering, The Hong Kong Polytechnic University, Hong Kong, China
[b] Shenzhen Institute of Advanced Electronic Materials, Shenzhen, China
[c] China Railway Inspection and Certification Center Co., Ltd., Beijing, 100081, China

ARTICLE INFO

Keywords:
Iron-based solid wastes
CO_2 adsorption
Carbon mineralization
Grand canonical Monte Carlo
Molecular dynamics

ABSTRACT

Iron-based alkaline solid wastes provide substrates for carbon mineralization, addressing global warming. However, the mechanisms of CO_2 transport and adsorption within their porous structures are not fully understood. Using advanced grand canonical Monte Carlo (GCMC) methods, this study explores CO_2 transport and adsorption in iron-based alkaline wastes under different humidity conditions. The results show that FeO and Fe_2O_3 reduce the CO_2 adsorption capacity in calcium hydroxide (CH) nanopores, a key component of these wastes. The presence of iron-based solids causes inhomogeneous porewater distribution, diminishing CO_2 dissolution and adsorption on the gas-liquid interface. By analyzing adsorption energy and CO_2 diffusion coefficients, we found that iron-based porous systems have lower CO_2 transport efficiency and storage capacity, highlighting their limited carbonation potential. The weak CO_2-surface interactions in these wastes are identified as the primary challenge to improving carbon mineralization. These findings provide crucial insights for enhancing the sustainable use of iron-based alkaline wastes.

1. Introduction

The exponential increase of global population and urbanization has led to an extensive demand for fossil fuels (Lin et al., 2024), resulting in the intensive discharge of greenhouse gases into the atmosphere (Caudle et al., 2023). Therefore, global polices stress the limitation of CO_2 emission (Change, 2021) and promotion of CO_2 capture and storage (CCS) (Metz et al., 2005). Among them, carbon mineralization has emerged as a promising strategy for CCS for its long-term security and favorable public acceptance (Matter et al., 2016). The concept of carbon mineralization originates from the utilization of natural ores, with a primary focus on the geologic formations (Romanov et al., 2015). These methods center around Ca/Mg-rich underground minerals, facilitating the permanent storage of CO_2 through the formation of carbonate minerals (Snæbjörnsdóttir et al., 2020). However, the intrinsically slow reaction kinetics and strict thermodynamics of carbonation reaction leads to the relatively low carbonation efficiency (Xie et al., 2015). Meanwhile, accelerated carbonation techniques using these nature ores typically require high-temperature and high-pressure conditions (Verduyn et al., 2011), resulting in elevated costs and energy input for activation, critically limiting the commercialization of these technologies (Matter et al., 2016). Alkaline solid wastes, owing to their abundance of alkaline-based components, emerge as promising candidates for carbon mineralization (Kravchenko et al., 2024; Pan et al., 2020; Yin et al., 2024). These alkaline solid wastes primarily stem from industrial residues, including combustion residues (Velts et al., 2011), mining/-mineral processing wastes (Harrison et al., 2013), cement/concrete wastes (Lu et al., 2024; Ostovari et al., 2021) and steelmaking slags (Pan et al., 2013). Among them, the steelmaking and cement industries are major contributors to the global CO_2 emission, demanding substantial energy input and resource exploitation (Jiang et al., 2023; Thonemann et al., 2022). Millions of tons of alkaline solid wastes are generated through these industrial activities. Therefore, harnessing cement and iron-based wastes for the long-term CO_2 storage could significantly expedite the achievement of the net-zero target, aligning with the principles of clean and sustainable production.

It is estimated that 310 million tons of CO_2 could be directly or indirectly sequestered (Liu et al., 2021) through the carbon mineralization, with 43.5% of this amount contributed by carbonation of steel slags. This process relies on the abundant alkaline metal ions present in

* Corresponding author.
** Corresponding author.
E-mail addresses: jia-xiang.liew@polyu.edu.hk (J. Liew), jia3huang@polyu.edu.hk (J. Huang).

https://doi.org/10.1016/j.dibe.2024.100595
Received 6 October 2024; Received in revised form 14 November 2024; Accepted 18 December 2024
Available online 25 December 2024

waste solids, including Ca^{2+} and Mg^{2+}. (Jiang et al., 2020; Zhang et al., 2023). Typically, the carbonation pathways involving steel slags are divided into two routes: direct mineral carbonation and indirect carbonation. Indirect carbonation methods achieve a higher carbonation conversion rate but necessitate a complex metal leaching and precipitation process involving acidic chemicals, which increases capital investment and pollution risks (Said et al., 2013). Direct carbonation sequesters CO_2 through carbonation reaction with calcium and magnesium oxide (e.g., CaO and MgO), silicates (e.g., Ca_3SiO_5 and Ca_2SiO_4.) (Azdarpour et al., 2015) and their hydroxides (e.g., $Ca(OH)_2$, $Mg(OH)_2$ and calcium silicate hydrate (C-S-H)) (Chen. et al., 2021b). These direct carbonation methods utilize metal oxides to sequester CO_2 through the solid-gas reactions (Bobicki et al., 2012). However, the kinetics of these reactions are very slow, and their thermodynamics favor occurrence at very high temperatures (Fagerlund et al., 2009), thereby intensively increasing the energy input.

On the other hand, aqueous carbonation methods exhibit markedly superior efficiency, which leverages solid-liquid-gas reaction at ambient temperature and moderate pressures (Ibrahim et al., 2019). Evolving from the fundamental principles of aqueous carbonation, accelerated carbonation techniques are proposed to further augment the carbonation efficiency (Song et al., 2021). Accelerated carbonation technology meticulously regulates parameters including temperature (Nielsen et al., 2020), CO_2 concentration and injecting pressure (Ko et al., 2015), relative humidity (RH) (Veetil and Hitch, 2020) to attain optimal CO_2 sequestration conditions. Notably, RH enhances the CO_2 transport and adsorption within the porous matrix of steel slags, expediting the release of cations such as Ca^{2+} and Mg^{2+} into the aqueous film on the moist solid surface, thereby enhancing CO_2 sequestration efficiency (Song et al., 2021). In the broader context of sustainability, this methodological finesse underscores the imperative for environmentally benign processes, positioning aqueous carbonation and its accelerated variants as instrumental in realizing cleaner and more sustainable carbon capture technologies.

To date, extensive research has been conducted on the accelerated carbonation of steel slags. However, current body of literature has not substantially advanced carbonation efficiency, primarily due to the absence of comprehensive bottom-up theories elucidating the mechanisms governing CO_2 transport and adsorption within these porous media, particularly at the micro and nano scales. Previous scientific inquiries have explored the impact of Relative Humidity (RH) on CO_2 adsorption within C-S-H nano channels (Zare et al., 2022). Nevertheless, in the context of steel slags, the presence of iron-based metal oxides (FeO and Fe_2O_3) significantly influences CO_2 transport and adsorption, aspects that remain inadequately addressed, impeding the progressive evolution of steel slags carbonation technologies. Traditional experimental methodologies prove inadequate in precisely capturing CO_2 adsorption and its intricate interactions with solid and liquid phases. In this work, we employed the advanced grand canonical Monte Carlo (GCMC) method to investigate the CO_2 transport and adsorption in the porous structure of alkaline solids, meticulously assessing the impact of FeO and Fe_2O_3 on the CO_2 adsorption within calcium hydroxide (CH) system. The elucidation of CO_2 storage efficiency and the characterization of the solid-solid interface functionality serve as pivotal contributions to the scientific discourse on developing clean and sustainable carbon capture technologies leveraging steel slag accelerated carbonation.

2. Methods

2.1. Model construction

To investigate the CO_2 transport and adsorption in nanopores of wasted iron-based alkaline solid, three different models are constructed as shown in Fig. 1. The first model denotes the general nano porous structure of alkaline solids, in which CH establishes the nano channel structures. The second and third model are built by the incorporation of FeO and Fe_2O_3 to investigate the effects of iron wastes. In each model, the solid substrates of CH, FeO and Fe_2O_3 are generated from their crystal unit cells. Then their supercells are obtained by expanding the x, y and z directions to create simulation boxes. The expanded structures are relaxed through NPT and NVT ensembles to reach the balanced energy state. Finally, their 001 surfaces are cleaved to build the 3 nm width nanopores. Although pore size of alkaline solids ranges from micro to nano scale, the nanosized pores majorly contributes to the carbonation reaction (Placencia-Gómez et al., 2020). The formation of wet surface provides the media for the dissolution of metal irons, CO_2 molecules and their reactions (Miller et al., 2019; Stack et al., 2014). Therefore, we focus on the nanopore, here, and employ 3 nm as the representative structure.

The thickness of water film also critically influences the CO_2 adsorption and transport. Here, we use 0–5 water layers to present moisture content ranging from 0 to 100 % with each layer representing an increase in 20 % moisture content of the alkaline solid system. The distance between each water layer is controlled by 0.23–0.29 nm, which is calculated from the density field of common water-solid system (Tao et al., 2022). When 5 water layers are added into 3 nm nanochannel, the channel is fully saturated with water film, exhibiting the 100% moisture content condition.

The relation between water layer thickness and RH can be calculated through Kelvin equation, which is written as

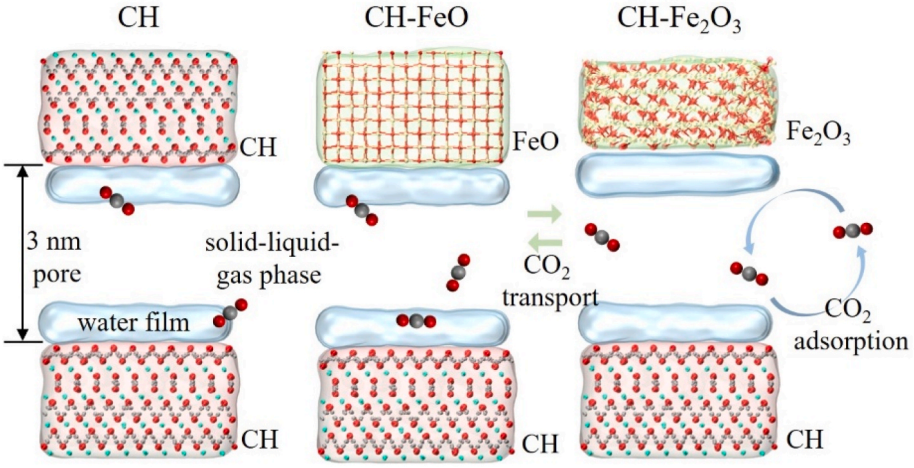

Fig. 1. Schematic illustration of molecular models of CH, CH-FeO and CH-Fe_2O_3 system for CO_2 adsorption and transport.

$$\ln\frac{p}{p_0} = -\frac{2\gamma V_m}{RT(d-2t)}, \quad (1)$$

where p and p_0 denote the actual and saturated vapor pressure. γ is the solid-liquid surface tension and V_m represents the molar volume of water. R and T are universal gas constant and temperature, respectively. $d-2t$ here is the modified pore size, in which t equals 0.23 nm to avoid the strong solid-liquid interactions of the first water layer.

2.2. Force field

ClayFF and CVFF force fields are employed to describe the solid-liquid-gas interactions in the entire simulation. In particular, ClayFF is used to describe CH, FeO, Fe_2O_3 and water film behaviors and CVFF is incorporated for the determination of the interaction between CO_2 and other phases. ClayFF has been widely used and shows strong capability in precisely capturing the atomic interactions in clay-based materials (Cygan et al., 2021), especially the solid-liquid interactions (Li et al., 2023a) and small molecule adsorptions (Li et al., 2023b) in these systems. The combination of ClayFF and CVFF has been explored and validated by (Cygan et al., 2012). Therefore, incorporating ClayFF and CVFF in our system is highly capable of investigating the CO_2 adsorption and transport in the alkaline porous system. All the parameters are shown in Table 1.

2.3. CO_2 adsorption

The CO_2 adsorption in nanopores of iron-incorporated alkaline solid highly depends on the adsorption pressure. In experimental studies, it is found that an injection pressure of 10 bar benefits accelerated carbonation while higher injection pressure barely further affects carbonation efficiency (Hyvert et al., 2010). Here we adopted the 10-bar pressure for CO_2 injection to keep a high computational efficiency and clearly observe the CO_2 quantity variation in nanopores. The chemical potential under different pressure can be calculated by

$$\mu_i = \mu_0 + RT\ln\frac{p}{p_0}, \quad (2)$$

where μ_0 equals −40 kJ/mol at 300 K and 1 bar. GCMC method is used in the simulation of CO_2 adsorption, which is a reliable tool applied in studying small molecules adsorption and transport (Honorio, 2019; Qomi et al., 2014; Zare et al., 2022). In our simulation, CO_2 molecules are inserted, removed or exchanged every 1 ps under NVT ensembles, after which another 1 ps NVT relaxation is utilized for the CO_2 molecules to freely transport in nanochannel. The total CO_2 adsorption continues for 2 ns to reach the fully adsorption state, during which the CO_2 quantity, distribution and energy variation are recorded every 1 ps. Finally, the adsorption properties in three systems are compared and analyzed.

The gaseous and dissolved CO_2 is determined by the coordinated number of C in CO_2 with respect to O in H_2O. To obtain the radius between CO_2 and H_2O, several CO_2 molecules are put into a large water box and freely moved to the equilibrium state. Then the radial distribution function (RDF) is tested as shown in Fig. 2(a). We select 5.2 Å as the coordination distance between CO_2 and H_2O molecules and calculate the average coordination number of CO_2 in water box. It can be observed from Fig. 2(b), the average coordination number of CO_2 with respect to H_2O oscillates around 11, thereby the coordination number of 11 is used to determine the dissolved and gaseous CO_2 molecules.

Table 1
Force Field parameters of modified CLAYFF and CVFF (Cygan et al., 2012).

Nonbonded potential			
Atom	q_i (e)	ε_{ij} (kcal/mol)	σ_{ij} (Å)
Ca	1.05	0.0000050298	5.566690
Och	−0.95	0.1554000000	3.170000
Hch	0.425	0.0000000000	0.000000
Ow	0.82	0.1554000000	3.170000
Hw	0.41	0.0000000000	0.000000
C	0.6512	0.0536490000	2.800000
Oc	−0.3256	0.1569730000	3.028000
Bond & Angle			
$k_{b\ O_w-H_w}$	554.197 kcal/mol	$r_{b\ O_w-H_w}$	1.0000 Å
$k_{a\ H_w-O_w-H_w}$	45.7696 kcal/mol	θ_0	109.47°
$k_{b\ C-O_c}$	1009.028 kcal/mol	$r_{b\ C-O_c}$	1.162 Å
$k_{a\ O_c-C-O_c}$	54.0500 kcal/mol	θ_0	180.00°

3. Results and discussion

For most alkaline solid wastes, the quantity of reactive Mg^{2+} and Ca^{2+} is the pivotal factor contributing to the carbonation capacity. Therefore, investigation of CO_2 transport and adsorption in CH nanopores exemplifies the carbon mineralization in alkaline solid wastes. Fig. 3(a) illustrates the total CO_2 adsorption in CH nanopores across varying RH. For the dry state (0 water layers), CO_2 molecules are consistently adsorbed into CH nanopores and reach the equilibrium state at 1.5 ns. Fig. 4(a–b) shows the gathering region of CO_2 molecules. Most of the CO_2 molecules concentrate on the solids surface due to the solid-gaseous attraction potentials. Concurrently, the CO_2 concentration on CH surface gradually increases (Fig. 4(b)) to the maximum quantity when the attraction potential equals to the CO_2 diffusion energy. On the other hand, only a few CO_2 molecules freely diffuse in the CH nano channel, which is determined by the injection pressures and temperatures. It has been experimentally demonstrated that increasing injection pressure from 1 to 10 bars could obviously promote the CO_2 carbonation while a higher pressure barely influences the further CO_2 adsorption (Fang et al., 2017; Fernández Bertos et al., 2004).

The humid environment progressively promotes the CO_2 adsorption in CH nanopores as referred in Fig. 3(a). With 3 and 4 water layers, the adsorbed CO_2 quantity reaches the maximum value. However, the CO_2 adsorption capacity of CH nanopores with high moisture content (5 water layers) sharply decreases. This result indicates that a moisture content around 60%–70% could significantly benefit the CO_2 accommodation by promoting the CO_2 adsorption capacity. Specifically, a low RH constructs a lower moisture content, exhibiting the thinner water film thickness, creating a large space for CO_2 transport while lowering CO_2 storage capacity (Fig. 4(c–d)). Conversely, a higher RH generates a thick water film, promoting the CO_2 storage capacity while hindering the CO_2 transport in nanopores due to the water film blocks nano channels.

Compared with CH nanopores, the Fe-incorporated nano porous system shows obvious differences. In the FeO-CH system, CO_2 adsorption capacity of dry channel shows similar values to that of CH system (shown in Fig. 3(b–c)). However, with the increment of water film thickness, the CO_2 storage capacity directly shrinks. A higher moisture content continuously limits CO_2 adsorption in such system, resulting in the maximum CO_2 adsorption capacity occurring at the totally dry state. The Fe_2O_3-CH system exhibits the similar CO_2 adsorption scenario, in which the increment of water film thickness hinders the CO_2 adsorption capacity. Experimental findings also reveal that decreasing the liquid to solid ratio benefits the CO_2 conversion rate in aqueous carbonation of steel slags (Huijgen et al., 2005; Song et al., 2021). The different effects of water films on CO_2 adsorption in these porous systems indicate the varying intrinsic properties of Fe-incorporated porous systems. However, mechanisms underlying these intricate phenomena remain elusive.

To further illustrate the effect of water film in each system, we compared the dissolved CO_2 quantity in three porous media (Fig. 5). In the 3 nm CH pores (Fig. 5(a)), the CO_2 amount in pore solution elevates with the increment of water layers. The total dissolved CO_2 quantity reaches the maximum with 4 water layers above CH solid surface. As shown in Fig. 4(d), with the increase of water film, several OH^- ions dissolve into the pore solution, which promotes the dissolution of CO_2 molecules. The full saturation (5 water layers) leads to the blockage of

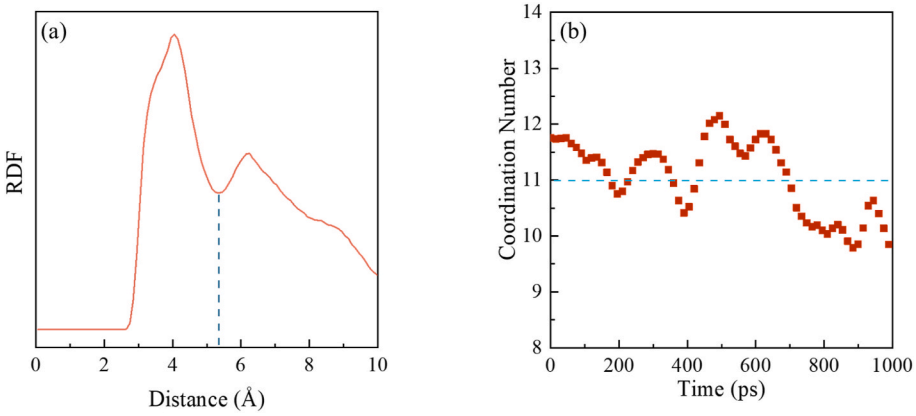

Fig. 2. (a) RDF of C-O; (b) coordination number of CO_2 in water box.

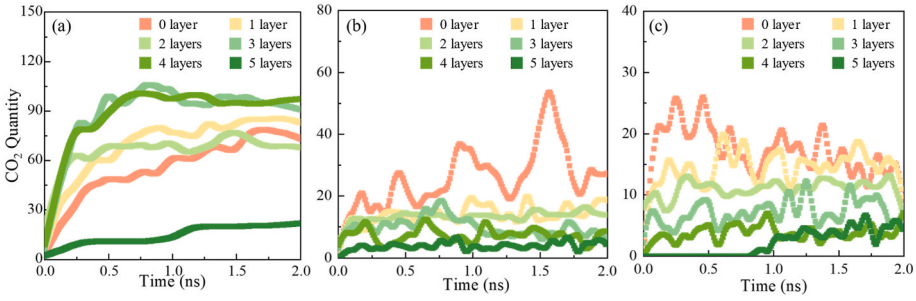

Fig. 3. Total CO_2 adsorption in different alkaline nanopores: (a) 3 nm CH pores; (b)3 nm FeO-CH pores and (c) 3 nm Fe_2O_3-CH pores.

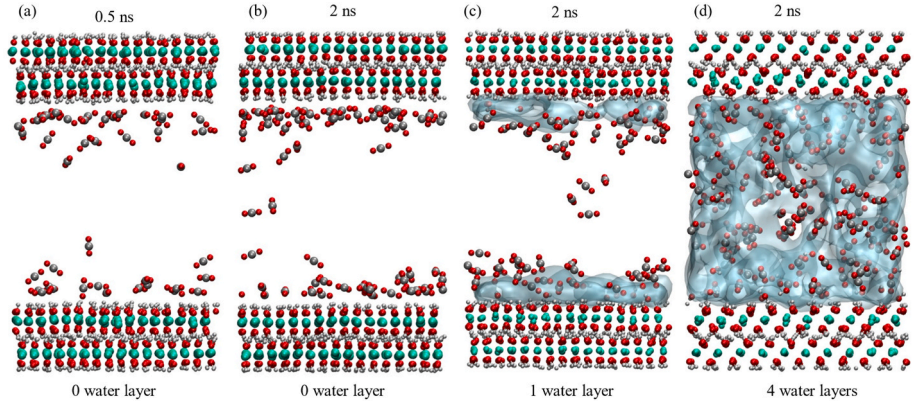

Fig. 4. Schematic illustration of CO_2 adsorption in 3 nm CH nanopores: (a) 0.5 ns within dry CH nanopores; (b) 2.0 ns within dry CH nanopores; (c) 2.0 ns within 1 water layer CH nanopores and (d) 2.0 ns within 4 water layers CH nanopores.

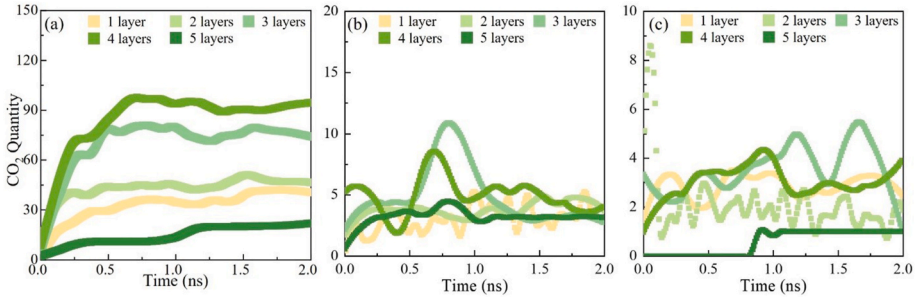

Fig. 5. Dissolved CO_2 quantity in nanopore solutions: (a) 3 nm CH pores; (b) 3 nm FeO-CH pores and (c) 3 nm Fe_2O_3-CH pores.

CO_2 transport, thereby drastically limiting the CO_2 adsorption in its channel. Compared with CH pore solution, water films within the Fe-incorporated CH system show a much lower CO_2 storage capacity (Fig. 5(b–c)). With the increment of water layers, the total CO_2 adsorption quantity barely changes in FeO-CH and Fe_2O_3-CH system. In these pore waters, the dissolved CO_2 quantity extensively varies, inferring that most of these dissolved CO_2 molecules exist at the liquid-gas interface. At these areas, gaseous and dissolved CO_2 molecules continuously transferred to each state, forming a dynamically equilibrium status. Such results indicate that the Fe-incorporated porous system creates a harsh environment for the dissolution of CO_2 molecules (Zare et al., 2022).

To further illustrate the Fe-incorporation effects on the pore solution, we depict the water distribution in Fig. 6. In 3 nm CH nanopores (Fig. 6 (a)), the water film symmetrically distributed along the Z direction. For 1 and 2 water layers, the peaks at 20 and 40 Å illustrate the concentrating layer of water films, where the range between the two peaks show the free gas region. With the increment of water layers, the peaks move to the middle part, showing the progressive shrinkage of free gas region. It should be noted that, some water molecules also evaporate into the free gas region as water vapors to reach the liquid-gas equilibrium, leading to the rise of trough. Compared with CH nanopores, the Fe-incorporated porous system shows an obvious uneven water distribution Fig. 6(b–c). Take FeO-CH system as an example, the water film symmetrically distributed with 1 water layer. However, the peaks on the left side become much higher than the right side when water layers reach 3. The shifted peaks illustrate the uneven distribution of porewater on two sides of nanopores, contributed by the water adsorption differences between CH, FeO and Fe_2O_3. Due to CH acquiring a more hydrophilic surface compared with FeO and Fe_2O_3, it attracts water molecules to aggregates on its side. Theoretical and experimental studies also demonstrated a much higher water adsorption energy (absolute value) of CH than FeO and Fe_2O_3 (Chen et al., 2021a; Joseph et al., 1999; Manzano et al., 2012). The uneven distribution of water film can be directly observed in Fig. 7, in which the nanopore media with 3 water layers are illustrated. In the CH nanopores, water film uniformly distributed, forming a large water-gas cluster. However, in the FeO-CH nanopore, most of the water layers are attracted to the CH side, while only leaving a thin water film on FeO side. Similar results can be seen in Fe_2O_3-CH nanopores, only a few water molecules are adsorbed on the Fe_2O_3 surface, whereas the majority of water film covers the entire CH surface, holding a high thickness.

The uneven distribution of water film definitely influences the CO_2 adsorption and transport in nanopores. Then we plot the CO_2 and water distribution in three nanopores to further investigate the porewater effects on CO_2 transport and adsorption. As shown in Fig. 8(a), CH nanopores holds the symmetrical distributed water films (green curve). Concurrently, the CO_2 distribution peaks appear in the inner side of water film, where the liquid-gas interface existed. As discussed, swift gaseous-dissolved CO_2 exchange occurs in these areas, leading to the CO_2 aggregation. The overlapping area denotes the dissolved CO_2 and the gaseous CO_2 molecules exist in the middle region where water films do not reach. These results show that gas/liquid interface is the CO_2 aggregated area. When water film thickness increases, a lot of gaseous CO_2 molecules mix with water molecules, forming the coexisted gas-liquid state in CH nanopores as shown in Fig. 7(a). Such state accelerates the liquid-gas mixing, significantly enhancing the contact area for CO_2 dissolution, thereby increasing the total CO_2 adsorption quantity. Similar in FeO-CH and Fe_2O_3-CH nanopores, the distribution peak shown is close to the peak of water films (Fig. 8(b–c)). However, due to the uneven distribution of water film, the CO_2 molecules barely occur in the porewater, whereas showing in the empty area not covered by water film. Fig. 7(b–c) illustrate the CO_2 distribution in Fe-incorporated nanopores. In these system, dissolved CO_2 disappears, with only gaseous CO_2 molecules remaining. Fe-incorporated nanopores lead to the uneven distribution of porewater so that diminishes the interaction area between CO_2 molecules and water film, thus significantly limiting the CO_2 adsorption quantity. The CH side with thicker water film hinders the CO_2 molecules to interact with CH surface, where abundant Ca^{2+} and OH^- ions concentrate. The thicker water film also lowers down the CO_2 molecules diffusion in solutions and carbonation reactions thus weakening its adsorption. On the other hand, the Fe side with thinner water film attracts CO_2 molecules based on interaction between CO_2 with FeO and Fe_2O_3 solid surface. However, the low carbonation reactivity of these components cannot attract high quantity of CO_2 molecules. Therefore, in these porous systems, most CO_2 molecules occur as gaseous state.

The CO_2 concentration in pore waters is analyzed as presented in Fig. 9. In the CH nanopores, the CO_2 concentration in the first water layer exhibits a much higher value. Such results come from the strong interaction between solid CH surface and CO_2 molecules, where the solid surface adsorption promotes the CO_2 dissolution in the thin water film. Theoretical investigation has identified the water condensation in nanopores caused by strong solid surface attractions and described such behaviors through Kelvin equation (Yang et al., 2020). With the increment of water layers, the solid surface attraction potential among CO_2 molecules sharply decreases, leading to the deterioration of CO_2 concentration in water film. When water layer reaches 5, the CO_2 concentration shows a much smaller value due to the low CO_2 transport efficiency, which limits the total CO_2 adsorption and dissolution quantity. Here, we can also find the critical value of CO_2 concentration in normal pore solutions, about 0.43 g/L in CH nanopores (referring to 2–4 water layers). This value is much higher than CO_2 dissolution in pure water (about 0.046 g/L) (Gilbert et al., 2016). Compared with CH nanopores, CO_2 concentration in pore solution of Fe-incorporate system exhibits much smaller value. The highest CO_2 concentration in FeO-CH and Fe_2O_3-CH nanopores is lower than 0.1 g/L, which is close to its dissolution concentration in pure water. The low CO_2 dissolve capacity in Fe-incorporated nanopores is highly related to the uneven distribution of porewater. On the CH side, accumulated water film prevent the solid-gas interactions. On the Fe side, few water film exists. Meanwhile the weak solid-gas interactions lead to the low CO_2 adsorption capacity. Therefore, in the Fe-incorporated alkaline solids, CO_2 molecules mainly exist as the form of gaseous state. Most of the CO_2 molecules in these nanopores are adsorbed on the solid surface, rather than dissolved in porewaters, thereby contributing to their weak CO_2 adsorption capacity.

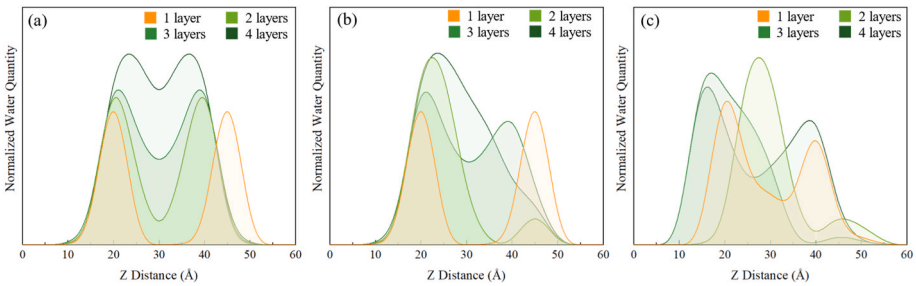

Fig. 6. Water film distribution in nanopore: (a) 3 nm CH pores; (b) 3 nm FeO-CH pores and (c) 3 nm Fe_2O_3-CH pores.

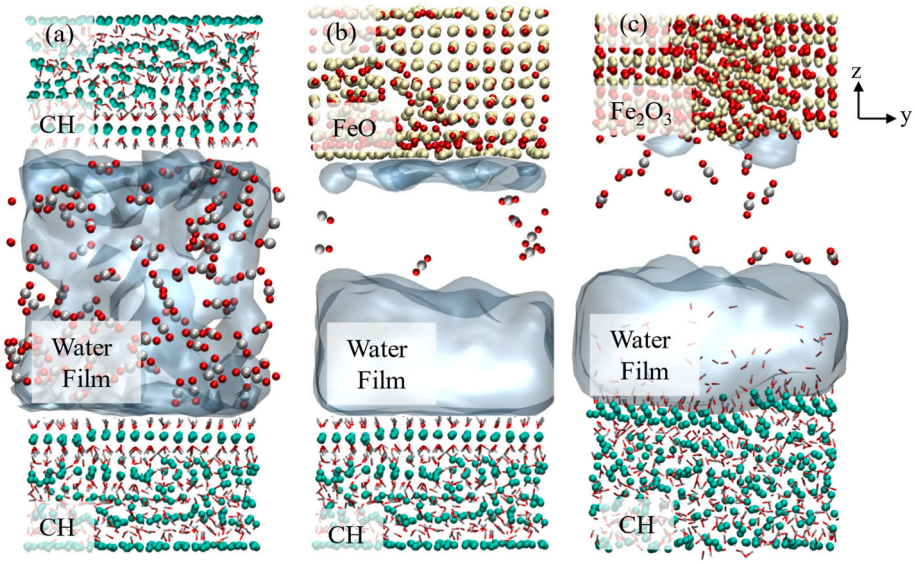

Fig. 7. Atomistic illustration of CO_2 adsorption in porous media at 2 ns: (a) 3 nm CH pores; (b) 3 nm FeO-CH pores and (c) 3 nm Fe_2O_3-CH pores.

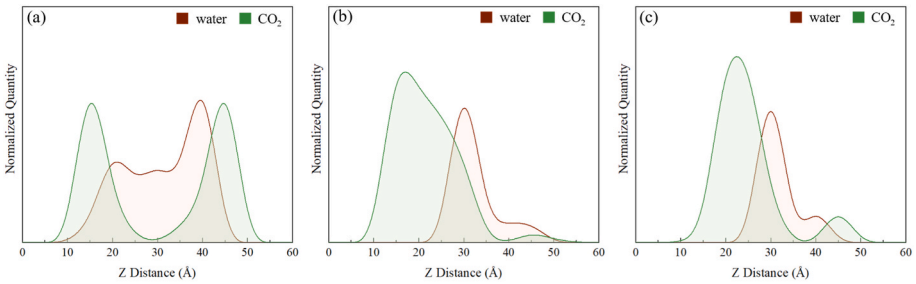

Fig. 8. Water film and CO_2 distribution in nanopore: (a) 3 nm CH pores; (b) 3 nm FeO-CH pores and (c) 3 nm Fe_2O_3-CH pores.

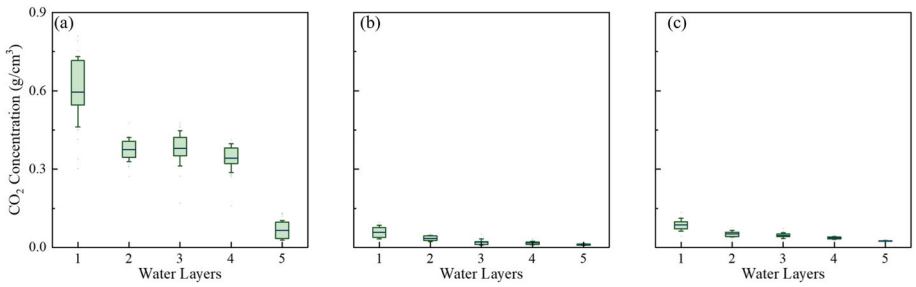

Fig. 9. CO_2 concentration in pore solutions: (a) 3 nm CH pores; (b) 3 nm FeO-CH pores and (c) 3 nm Fe_2O_3-CH pores.

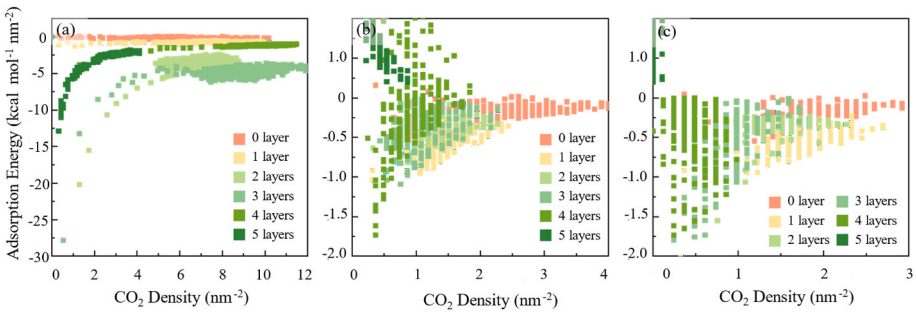

Fig. 10. CO_2 adsorption energy in porous system: (a) 3 nm CH pores; (b) 3 nm FeO-CH pores and (c) 3 nm Fe_2O_3-CH pores.

To further illustrate the CO_2 adsorption capacities in these systems, we calculate the CO_2 adsorption energy in 3 nm nanopores with varying water layers as shown in Fig. 10. It can be observed that with the increment of water layers, the CH nanopores acquire a higher CO_2 adsorption energy (absolute value). The adsorption energy of first several CO_2 molecules in 3 and 4 water layers is lower than −25 kcal/(mol·nm^2), indicating a strong CO_2 adsorption capacity. With the accumulation of CO_2 on the surface, the adsorption energy gradually decreases, until the equilibrium state is established. The stable adsorption energy shows an identical tendency with respect to total CO_2 adsorption quantities. The CO_2 adsorption energy at equilibrium state is enhanced with the growth of water layer in nanopores, indicating the optimal water layers benefit the CO_2 adsorption in CH nanopores. Contradictory results are found in Fe-incorporated system (Fig. 10 (b–c)). The adsorption energy of CO_2 in FeO-CH and Fe_2O_3-CH channel is much smaller than that in CH nanopores, which explains their weak CO_2 adsorption capacities. Particularly, the CO_2 adsorption energy in both Fe-incorporated systems is higher than −2.0 kcal/(mol·nm^2), testifying such system can barely adsorb CO_2 in its channel. Due to the low adsorption capacity, the density of CO_2 only reaches 3 nm^{-2}, most of which forms as the gaseous state. These results demonstrate that CO_2 molecules in Fe-incorporated nanopores are hard to be adsorbed on their wet solid surface, and instead freely diffuse as gaseous state. Besides, when water layers are higher than 4, the adsorption energy in such system becomes positive, showing as the repulsive interactions, thereby significantly preventing the dissolution of CO_2 molecules in pore solution.

The transport behaviors of CO_2 molecules in nanopores are characterized through their diffusion coefficients. As shown in Fig. 11(a), CO_2 diffusion coefficient (D_{CO2}) in CH nanopores varies with different water layers. The highest D_{CO2} reaches with respect to 3 water layers. At low water thickness, the CO_2 diffusion is limited by both solid surface attraction as well as water dissolution, therefore the dry surface shows a higher D_{CO2} than 1 water layer. With the increase of water layer, the solid surface attraction diminishes so that CO_2 diffusion is only controlled by water dissolution. At 3 water layers, the CO_2 intensive exchange occurs between liquid and gas state so that the D_{CO2} reaches the maximum value. For the 4 and 5 water layers, the CH channel is filled with water films, leaving little space for gaseous CO_2 diffusion, thereby D_{CO2} in these systems sharply decreasing. In the FeO-CH and Fe_2O_3-CH systems, CO_2 molecules barely dissolve into the porewater, according to the CO_2 adsorption energies. Besides, the solid surface attraction is also weak. Therefore, the CO_2 diffusion is only affected by the pore size. With the increase of water layer, empty space available for gaseous CO_2 free diffusion becomes smaller and smaller, so that D_{CO2} in these systems continuously decreases. It should be noted that, D_{CO2} in Fe-incorporated system is much smaller than that in CH nanopores. This can be explained by the weak CO_2 adsorption and dissolution capacity of Fe-incorporated system. Liquid-gas exchanges in these systems provide high dynamic energy for CO_2 molecules and providing them thermodynamic potentials. Due to much smaller quantity of dissolved CO_2 in Fe-incorporated nanochannel, liquid-gas transition barely occurs in these systems so that the adsorbed CO_2 molecules are not activated to participate into the heat and thermodynamic exchange, leading to the much lower D_{CO2} in these systems.

4. Conclusion

In this work, we employ the advanced GCMC method to meticulously probe the intricate dynamics of CO_2 transport and adsorption within the nanopores of alkaline solids. We systemically compared the CO_2 adsorption capacity and transport efficiency in CH and iron-incorporated alkaline systems under varying RH conditions. A notable reduction in the total CO_2 adsorption amount upon the integration of FeO and Fe_2O_3 highlights the significant impact of iron incorporation on CO_2 capture efficiency. Furthermore, CO_2 solubility within the porewater of FeO and Fe_2O_3 systems was considerably diminished due to the creation of weak alkaline environments. Concurrently, the distinct water adsorption capacity between CH and iron-based solids results in an uneven distribution of porewater. The strong solid-liquid interactions observed in CH side lead to the formation of thicker water films, which not only attenuates the surface affinity for CO_2 molecules but also impedes carbonation reactions by reducing CO_2 diffusion efficiency. In the context of FeO and Fe_2O_3, weak solid-water interactions result in significantly reduced water film thickness. Coupled with weak solid-gas interactions, this phenomenon limits the adsorption of CO_2 molecules within Fe-incorporated nanopores, predominantly maintaining them in a gaseous state, with the majority dissolving in CH porewater. These findings provide valuable insights into the disparities of CO_2 transport and storage in varying alkaline solids systems, thus contributing to the development of sustainable strategies for their effective carbon mineralization.

Through comparative analysis across varying humidity levels, we observed shifts in porewater thickness from complete dryness to full saturation. While CO_2 adsorption in CH nanopores demonstrates an optimal water thickness, elevated water content progressively diminishes CO_2 adsorption in Fe-incorporated nanopore systems due to its poor solubility. Further studies underscore that iron-based alkaline solids exhibit much lower CO_2 adsorption energy and diffusion coefficient, providing empirical support for their diminished carbonation efficiency. This work provides bottom-up pictures of CO_2 adsorption and transport in iron-based alkaline solids, elucidating the mechanisms of low carbonation efficiency in iron-based materials, with implications for the development of sustainable and environmentally sound waste management strategies. By elucidating the intricate interplay between solid-water-gas interactions, this research advances our understanding

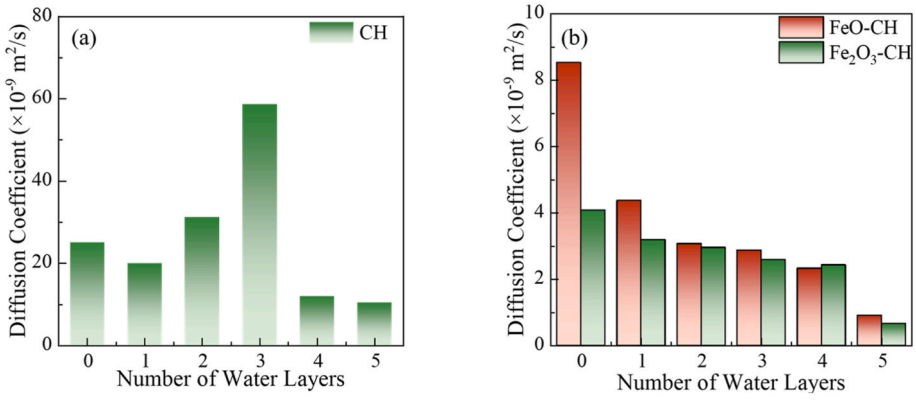

Fig. 11. CO_2 diffusion coefficient in porous system: (a) 3 nm CH pores and (b) 3 nm FeO-CH pores and 3 nm Fe_2O_3-CH pores.

of CO_2 sequestration mechanisms within iron-based alkaline solids, thereby informing the design of more effective and sustainable carbon mineralization methods.

Future work focuses on the extension of the current study to various alkaline minerals, searching for the optimal alkaline solids for CO_2 adsorption and carbon mineralization. A large-scale simulation will be conducted and a database for varying minerals will be established. Then, the simulated data would be utilized to guide the experimental studies, finding out the most effective alkaline solids for practical CCS.

CRediT authorship contribution statement

Gen Li: Writing – original draft, Methodology, Formal analysis, Conceptualization. **Jie Yang:** Formal analysis. **Hao Li:** Resources, Methodology. **Jiaxiang Liew:** Writing – original draft, Formal analysis. **Jiasheng Huang:** Writing – review & editing, Supervision, Conceptualization.

Declaration of competing interest

The authors declare that they have no known competing financial interests or personal relationships that could have appeared to influence the work reported in this paper.

Data availability

Data will be made available on request.

References

Azdarpour, A., Asadullah, M., Mohammadian, E., Hamidi, H., Junin, R., Karaei, M.A., 2015. A review on carbon dioxide mineral carbonation through pH-swing process. Chem. Eng. J. 279, 615–630.

Bobicki, E.R., Liu, Q., Xu, Z., Zeng, H., 2012. Carbon capture and storage using alkaline industrial wastes. Prog. Energy Combust. Sci. 38 (2), 302–320.

Caudle, B., Taniguchi, S., Nguyen, T.T.H., Kataoka, S., 2023. Integrating carbon capture and utilization into the glass industry: Economic analysis of emissions reduction through CO2 mineralization. J. Clean. Prod. 416, 137846.

Change, U.C., 2021. The Glasgow climate pact–key outcomes from COP26. UNFCCC Sites and Platforms.

Chen, C., Zhao, C., Zhou, X., Chen, J., Chen, L., Li, F., 2021a. DFT study on the interaction of H2O and O2 with α-Fe2O3 (001) surface. Vacuum 188, 110164.

Chen, Z., Cang, Z., Yang, F., Zhang, J., Zhang, L., 2021b. Carbonation of steelmaking slag presents an opportunity for carbon neutral: a review. J. CO2 Util. 54, 101738.

Cygan, R.T., Greathouse, J.A., Kalinichev, A.G., 2021. Advances in Clayff molecular simulation of layered and nanoporous materials and their aqueous interfaces. J. Phys. Chem. C 125 (32), 17573–17589.

Cygan, R.T., Romanov, V.N., Myshakin, E.M., 2012. Molecular simulation of carbon dioxide capture by Montmorillonite using an Accurate and Flexible force field. J. Phys. Chem. C 116 (24), 13079–13091.

Fagerlund, J., Teir, S., Nduagu, E., Zevenhoven, R., 2009. Carbonation of magnesium silicate mineral using a pressurised gas/solid process. Energy Proc. 1 (1), 4907–4914.

Fang, X., Xuan, D., Poon, C.S., 2017. Empirical modelling of CO2 uptake by recycled concrete aggregates under accelerated carbonation conditions. Mater. Struct. 50 (4), 200.

Fernández Bertos, M., Simons, S.J.R., Hills, C.D., Carey, P.J., 2004. A review of accelerated carbonation technology in the treatment of cement-based materials and sequestration of CO2. J. Hazard Mater. 112 (3), 193–205.

Gilbert, K., Bennett, P.C., Wolfe, W., Zhang, T., Romanak, K.D., 2016. CO2 solubility in aqueous solutions containing Na+, Ca2+, Cl−, SO42− and HCO3-: the effects of electrostricted water and ion hydration thermodynamics. Appl. Geochem. 67, 59–67.

Harrison, A.L., Power, I.M., Dipple, G.M., 2013. Accelerated carbonation of brucite in mine tailings for carbon sequestration. Environmental science & technology 47 (1), 126–134.

Honorio, T., 2019. Monte Carlo molecular modeling of temperature and pressure effects on the interactions between Crystalline calcium silicate hydrate layers. Langmuir 35 (11), 3907–3916.

Huijgen, W.J., Witkamp, G.-J., Comans, R.N., 2005. Mineral CO2 sequestration by steel slag carbonation. Environmental science & technology 39 (24), 9676–9682.

Hyvert, N., Sellier, A., Duprat, F., Rougeau, P., Francisco, P., 2010. Dependency of C–S–H carbonation rate on CO2 pressure to explain transition from accelerated tests to natural carbonation. Cement Concr. Res. 40 (11), 1582–1589.

Ibrahim, M.H., El-Naas, M.H., Benamor, A., Al-Sobhi, S.S., Zhang, Z., 2019. Carbon mineralization by reaction with steel-making waste: a review. Processes 7 (2), 115.

Jiang, X., Xiao, R., Ma, Y., Zhang, M., Bai, Y., Huang, B., 2020. Influence of waste glass powder on the physico-mechanical properties and microstructures of fly ash-based geopolymer paste after exposure to high temperatures. Construct. Build. Mater. 262, 120579.

Jiang, X., Zhang, Y., Zhang, Y., Ma, J., Xiao, R., Guo, F., Bai, Y., Huang, B., 2023. Influence of size effect on the properties of slag and waste glass-based geopolymer paste. J. Clean. Prod. 383, 135428.

Joseph, Y., Kuhrs, C., Ranke, W., Ritter, M., Weiss, W., 1999. Adsorption of water on FeO (111) and Fe3O4(111): identification of active sites for dissociation. Chem. Phys. Lett. 314 (3), 195–202.

Ko, M.-S., Chen, Y.-L., Jiang, J.-H., 2015. Accelerated carbonation of basic oxygen furnace slag and the effects on its mechanical properties. Construct. Build. Mater. 98, 286–293.

Kravchenko, E., Lazorenko, G., Jiang, X., Leng, Z., 2024. Alkali-activated materials made of construction and demolition waste as precursors: a review. Sustainable Materials and Technologies 39, e00829.

Li, G., Akbar, A., Zhang, L.-W., Rosei, F., Liew, K.M., 2023a. Surface modification strategy for controlling wettability and ionic diffusion behaviors of calcium silicate hydrate. Appl. Surf. Sci. 622, 156993.

Li, G., Yin, B., Zhang, L., Liew, K., 2023b. The hydraulic interface towards the anti-fatigue performance of fiber-calcium silicate hydrate composites under cyclic loading. Compos. Appl. Sci. Manuf. 171, 107579.

Lin, X., Zhang, Y., Liu, H., Boczkaj, G., Cao, Y., Wang, C., 2024. Carbon dioxide sequestration by industrial wastes through mineral carbonation: current status and perspectives. J. Clean. Prod. 434, 140258.

Liu, W., Teng, L., Rohani, S., Qin, Z., Zhao, B., Xu, C.C., Ren, S., Liu, Q., Liang, B., 2021. CO2 mineral carbonation using industrial solid wastes: a review of recent developments. Chem. Eng. J. 416, 129093.

Lu, D., Jiang, X., Qu, F., Huo, Y., 2024. Mitigating sulfate ions migration in concrete: a targeted approach to address recycled concrete aggregate's impact. J. Clean. Prod. 442, 141135.

Manzano, H., Pellenq, R.J.M., Ulm, F.-J., Buehler, M.J., van Duin, A.C.T., 2012. Hydration of calcium oxide surface Predicted by reactive force field molecular dynamics. Langmuir 28 (9), 4187–4197.

Matter, J.M., Stute, M., Snæbjörnsdottir, S.Ó., Oelkers, E.H., Gislason, S.R., Aradottir, E. S., Sigfusson, B., Gunnarsson, I., Sigurdardottir, H., Gunnlaugsson, E., 2016. Rapid carbon mineralization for permanent disposal of anthropogenic carbon dioxide emissions. Science 352 (6291), 1312–1314.

Metz, B., Davidson, O., De Coninck, H., Loos, M., Meyer, L., 2005. IPCC Special Report on Carbon Dioxide Capture and Storage. Cambridge University Press, Cambridge.

Miller, Q.R., Kaszuba, J.P., Schaef, H.T., Bowden, M.E., McGrail, B.P., Rosso, K.M., 2019. Anomalously low activation energy of nanoconfined MgCO 3 precipitation. Chem. Commun. 55 (48), 6835–6837.

Nielsen, P., Boone, M., Horckmans, L., Snellings, R., Quaghebeur, M., 2020. Accelerated carbonation of steel slag monoliths at low CO2 pressure–microstructure and strength development. J. CO2 Util. 36, 124–134.

Ostovari, H., Muller, L., Skocek, J., Bardow, A., 2021. From unavoidable CO2 source to CO2 sink? A cement industry based on CO2 mineralization. Environmental science & technology 55 (8), 5212–5223.

Pan, S.-Y., Chen, Y.-H., Fan, L.-S., Kim, H., Gao, X., Ling, T.-C., Chiang, P.-C., Pei, S.-L., Gu, G., 2020. CO2 mineralization and utilization by alkaline solid wastes for potential carbon reduction. Nat. Sustain. 3 (5), 399–405.

Pan, S.-Y., Chiang, P.-C., Chen, Y.-H., Tan, C.-S., Chang, E.E., 2013. Ex Situ CO2 capture by carbonation of steelmaking slag Coupled with Metalworking Wastewater in a Rotating Packed bed. Environmental Science & Technology 47 (7), 3308–3315.

Placencia-Gómez, E., Kerisit, S.N., Mehta, H.S., Qafoku, O., Thompson, C.J., Graham, T. R., Ilton, E.S., Loring, J.S., 2020. Critical water coverage during Forsterite carbonation in thin water films: Activating dissolution and Mass transport. Environmental Science & Technology 54 (11), 6888–6899.

Qomi, M.A., Krakowiak, K., Bauchy, M., Stewart, K., Shahsavari, R., Jagannathan, D., Brommer, D.B., Baronnet, A., Buehler, M.J., Yip, S., 2014. Combinatorial molecular optimization of cement hydrates. Nat. Commun. 5 (1), 1–10.

Romanov, V., Soong, Y., Carney, C., Rush, G.E., Nielsen, B., O'Connor, W., 2015. Mineralization of carbon dioxide: a literature review. ChemBioEng Rev. 2 (4), 231–256.

Said, A., Mattila, H.-P., Järvinen, M., Zevenhoven, R., 2013. Production of precipitated calcium carbonate (PCC) from steelmaking slag for fixation of CO2. Appl. Energy 112, 765–771.

Snæbjörnsdóttir, S.Ó., Sigfússon, B., Marieni, C., Goldberg, D., Gislason, S.R., Oelkers, E. H., 2020. Carbon dioxide storage through mineral carbonation. Nat. Rev. Earth Environ. 1 (2), 90–102.

Song, Q., Guo, M.-Z., Wang, L., Ling, T.-C., 2021. Use of steel slag as sustainable construction materials: a review of accelerated carbonation treatment. Resour. Conserv. Recycl. 173, 105740.

Stack, A.G., Fernandez-Martinez, A., Allard, L.F., Banuelos, J.L., Rother, G., Anovitz, L. M., Cole, D.R., Waychunas, G.A., 2014. Pore-size-dependent calcium carbonate precipitation controlled by surface chemistry. Environmental science & technology 48 (11), 6177–6183.

Tao, Y., Zare, S., Wang, F., Qomi, M.J.A., 2022. Atomistic thermodynamics and kinetics of dicalcium silicate dissolution. Cement Concr. Res. 157, 106833.

Thonemann, N., Zacharopoulos, L., Fromme, F., Nühlen, J., 2022. Environmental impacts of carbon capture and utilization by mineral carbonation: a systematic literature review and meta life cycle assessment. J. Clean. Prod. 332, 130067.

Veetil, S., Hitch, M., 2020. Recent developments and challenges of aqueous mineral carbonation: a review. Int. J. Environ. Sci. Technol. 17, 4359–4380.

Velts, O., Uibu, M., Kallas, J., Kuusik, R., 2011. Waste oil shale ash as a novel source of calcium for precipitated calcium carbonate: carbonation mechanism, modeling, and product characterization. J. Hazard Mater. 195, 139–146.

Verduyn, M., Geerlings, H., van Mossel, G., Vijayakumari, S., 2011. Review of the various CO2 mineralization product forms. Energy Proc. 4, 2885–2892.
Xie, H., Yue, H., Zhu, J., Liang, B., Li, C., Wang, Y., Xie, L., Zhou, X., 2015. Scientific and engineering progress in CO2 mineralization using industrial waste and natural minerals. Engineering 1 (1), 150–157.
Yang, Q., Sun, P., Fumagalli, L., Stebunov, Y., Haigh, S., Zhou, Z., Grigorieva, I., Wang, F., Geim, A., 2020. Capillary condensation under atomic-scale confinement. Nature 588 (7837), 250–253.
Yin, B., Huang, J., Sun, W., 2024. Peridynamics-fueled convolutional neural network for predicting mechanical constitutive behaviors of fiber reinforced composites. Comput. Methods Appl. Mech. Eng. 431, 117309.
Zare, S., Uddin, K.S., Funk, A., Miller, Q.R., Qomi, M.J.A., 2022. Nanoconfinement matters in humidified CO 2 interaction with metal silicates. Environ. Sci.: Nano 9 (10), 3766–3779.
Zhang, Y., Yu, L., Cui, K., Wang, H., Fu, T., 2023. Carbon capture and storage technology by steel-making slags: recent progress and future challenges. Chem. Eng. J. 455, 140552.